One-Pot Synthesized Bicontinuous Hierarchical Li$_3$V$_2$(PO$_4$)$_3$/C Mesoporous Nanowires for High-Rate and Ultralong-Life Lithium-ion Batteries

Qiulong Wei,[†,§] Qinyou An,[†,§] Dandan Chen,[†,§] Liqiang Mai,*[,†] Shiyu Chen,[†] Yunlong Zhao,[†] Kalele Mulonda Hercule,[†] Lin Xu,[†,‡] Aamir Minhas-Khan,[†] and Qingjie Zhang[†]
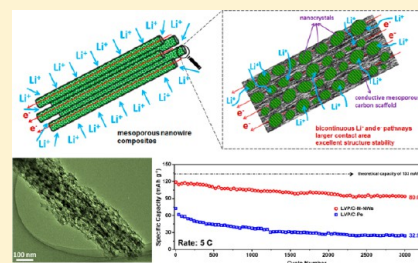
[†]State Key Laboratory of Advanced Technology for Materials Synthesis and Processing, WUT-Harvard Joint Nano Key Laboratory, Wuhan University of Technology, Wuhan 430070, China

[‡]Department of Chemistry and Chemical Biology, Harvard University, Cambridge, Massachusetts 02138, United States

Ⓢ Supporting Information

ABSTRACT: Lithium-ion batteries have attracted enormous attention for large-scale and sustainable energy storage applications. Here we present a design of hierarchical Li$_3$V$_2$(PO$_4$)$_3$/C mesoporous nanowires via one-pot synthesis process. The mesoporous structure is directly *in situ* carbonized from the surfactants (CTAB and oxalic acid) along with the crystallization of Li$_3$V$_2$(PO$_4$)$_3$ without using any hard templates. As a cathode for lithium-ion battery, the Li$_3$V$_2$(PO$_4$)$_3$/C mesoporous nanowires exhibit outstanding high-rate and ultralong-life performance with capacity retention of 80.0% after 3000 cycles at 5 C in 3−4.3 V. Even at 10 C, it still delivers 88.0% of its theoretical capacity. The ability to provide this level of performance is attributed to the hierarchical mesoporous nanowires with bicontinuous electron/ion pathways, large electrode−electrolyte contact area, low charge transfer resistance, and robust structure stability upon prolonged cycling. Our work demonstrates that the unique mesoporous nanowires structure is favorable for improving the cyclability and rate capability in energy storage applications.

KEYWORDS: Nanowire, mesoporous structure, hierarchical structure, bicontinuous pathways, lithium-ion batteries, Li$_3$V$_2$(PO$_4$)$_3$

Rechargeable lithium-ion batteries (LIBs) have been rapidly developed for applications in hybrid electric vehicles (HEVs), electric vehicles (EVs), and large-scale energy storage due to their high energy density and durable cycle life.[1−6] From the viewpoint of electrode materials, lithium transition-metal phosphates have attracted tremendous attention as cathodes for rechargeable LIBs.[7−10] Among the phosphate compounds, monoclinic Li$_3$V$_2$(PO$_4$)$_3$ (LVP) is proposed as a highly prospective cathode, owing to its high operating voltage, large theoretical specific capacity, thermodynamically stable structure, and abundance in nature.[8−11] However, the LVP exhibits inferior electron conductivity due to the two separated [VO$_6$] octahedral arrangement, which limits its widespread applications.[12−15] Coating conductive carbon[16−18] can overcome the low electron conductivity of electrode materials, while irregular coatings may lead to poor connectivity of the particles and hence capacity loss. Further, as proposed by Braun and his co-workers, an approach of combining active electrode materials with conductive scaffolds can largely enhance the electron transport and the electrochemical performance.[19]

In addition, for a lithium storage process it involves not only electron transport but also ion diffusion in the electrode materials. To further achieve high-rate capability the ion diffusion kinetics needs to be enhanced. According to the diffusion formula $t = L^2/D$ (where t is the ion diffusion time, L is the ion diffusion length, and D is the ion diffusion

coefficient), synthesizing electrode materials within nanosize is one of the most effective strategies to shorten the ion diffusion distance and then improve the rate performance.[2−6,19] Among the wide range of nanostructures, nanowires with unique electronic and structural properties have exhibited lots of advantages in energy applications.[20,21] For LIBs, the nanowires provide short ion diffusion distance as well as continuous electron transport pathway, which have demonstrated the superiority in energy storage applications.[6,22−27] Besides, porous structure can largely increase the contact area between electrode and electrolyte, which effectively facilitates the ion diffusion kinetics.[27−33] Also, the porous structure provides more space for the volume changes during charge/discharge, improving their cyclability.[30−33] Thus, as illustrated in Figure 1a, constructing a hierarchical mesoporous nanowire composite with active nanocrystals and conductive mesoporous nanowire scaffolds can provide large surface area, rapid ion/electron transport, and excellent structure stability, resulting in outstanding lithium storage performance. Previously, mesoporous LiFePO$_4$,[30] Li$_4$Ti$_5$O$_{12}$,[31] MoS$_2$,[32] and MoSe$_2$[33] have been synthesized via nanocasting method and display good rate capacity and cyclability. However, the multistep process
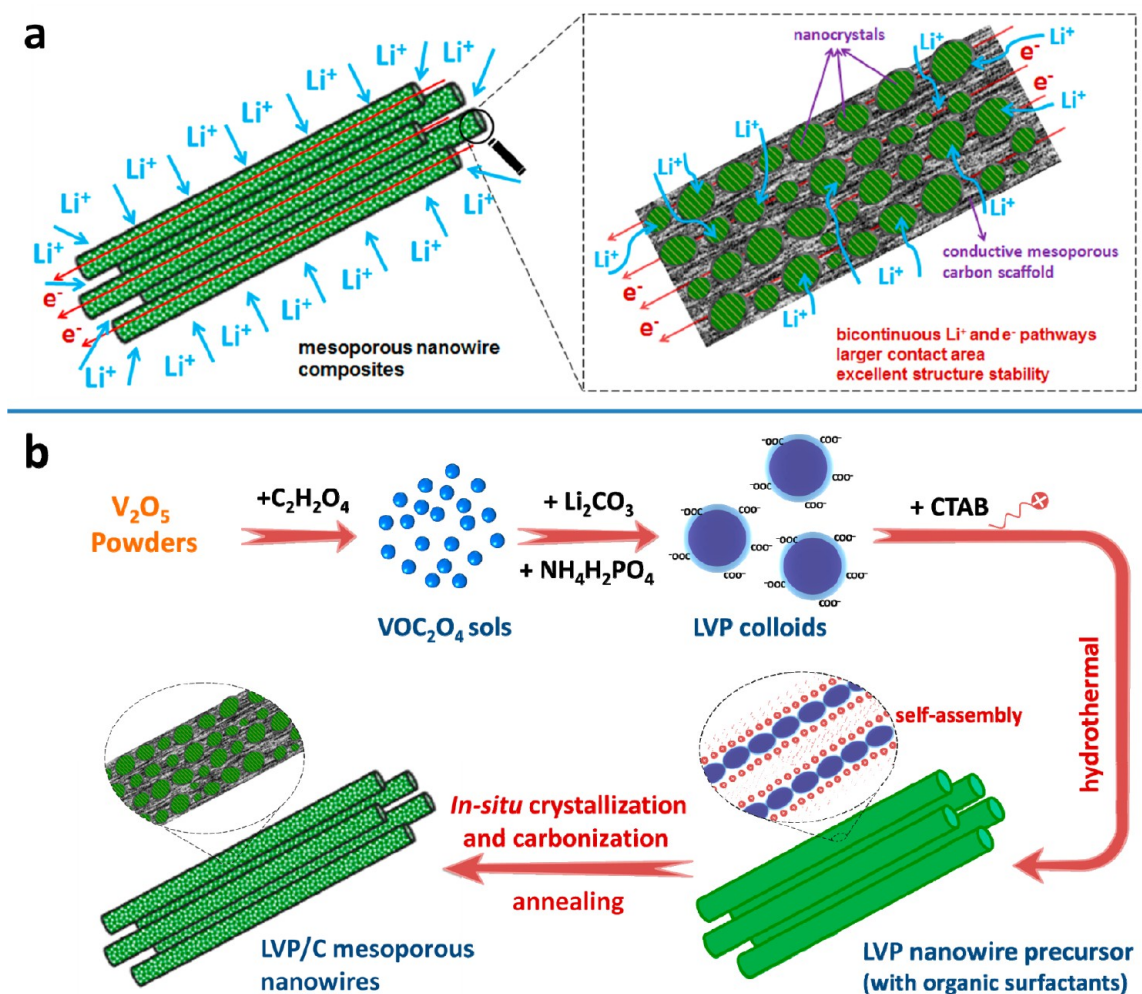
Figure 1. (a) Schematic illustration of the mesoporous nanowire composites with bicontinuous electron/ion transport pathways, larger electrode–electrolyte contact area, and facile strain relaxation during Li⁺ extractrion/insertion. (b) Schematic illustration of the fabrication steps and proposed formation mechanism for the LVP/C-M-NWs.

including the synthesis and/or removal of hard template may increase preparation costs.[34] Therefore, it is challenging but significant to develop a facile method for synthesizing mesoporous composites.[30,31] To the best of our knowledge, a rational one-pot synthesis of LVP/C mesoporous nanowire structures is rarely reported and remain largely unexplored.

Herein, we present a one-pot synthesis of hierarchical LVP/C mesoporous nanowires (LVP/C-M-NWs) via hydrothermal and annealing treatment. The cetyltrimethylammonium bromide (CTAB) and oxalic acid are simultaneously used as surfactant and carbon sources to form the mesoporous carbon scaffolds along with the crystallization of LVP. During the *in situ* crystallization and carbonization process, the nanocrystals can be embedded in the conductive scaffold, which endows the effective electron contacts. As cathode for LIBs, the hierarchical structure endows the LVP/C-M-NWs with largely enhanced rate capability and cycling stability, compared to the simple carbon-coated LVP particles (LVP/C-Ps) and pure LVP particles (LVP-Ps).

Briefly, Figure 1b schematically illustrates the fabrication steps and proposed formation mechanism of LVP/C-M-NWs. First, VOC_2O_4 sols were prepared by dissolving V_2O_5 and oxalic acid in deionized water at 70 °C (Supporting Information Figure S1a).[35] Second, the mixed Li_2CO_3 and

$NH_4H_2PO_4$ solution was added into the prepared VOC_2O_4 sols to form LVP hydrophilic homogeneous colloids with anionic surface. Third, driven by Coulomb force, the added cationic surfactant CTAB captured the anionic LVP colloids, which rearranged the charge density and formed composite micelles in the solution.[36,37] During hydrothermal process, the organic molecules located in the interstitial space of the aggregated composite assembled into mesochannels.[38] Meanwhile the self-assembly of organic surfactants and the hydrolysis of LVP colloids resulted in the nanowire morphology (Figure 2a).[39,40] Finally, the as-prepared nanowire precursor was annealed to crystallize the LVP with the release and *in situ* carbonization of organic compounds, along with large mass loss (Supporting Information Figure S2). Homogeneous micelles with charged surface are very important to control the surface curvature and self-assembly process.[37,40] Without adding CTAB into the LVP hydrophilic homogeneous sols, the LVP sols turn into blue LVP hydrogel after hydrothermal treatment (Supporting Information Figures S1b). And the LVP/C-Ps were obtained by annealing the dried hydrogel (Supporting Information Figures S3). Meanwhile, without adding oxalic acid to form the hydrophilic homogeneous sols and by only adding CTAB, the nanowires were not formed similarly (Supporting Information Figure S4). As a control experiment, the LVP-Ps were
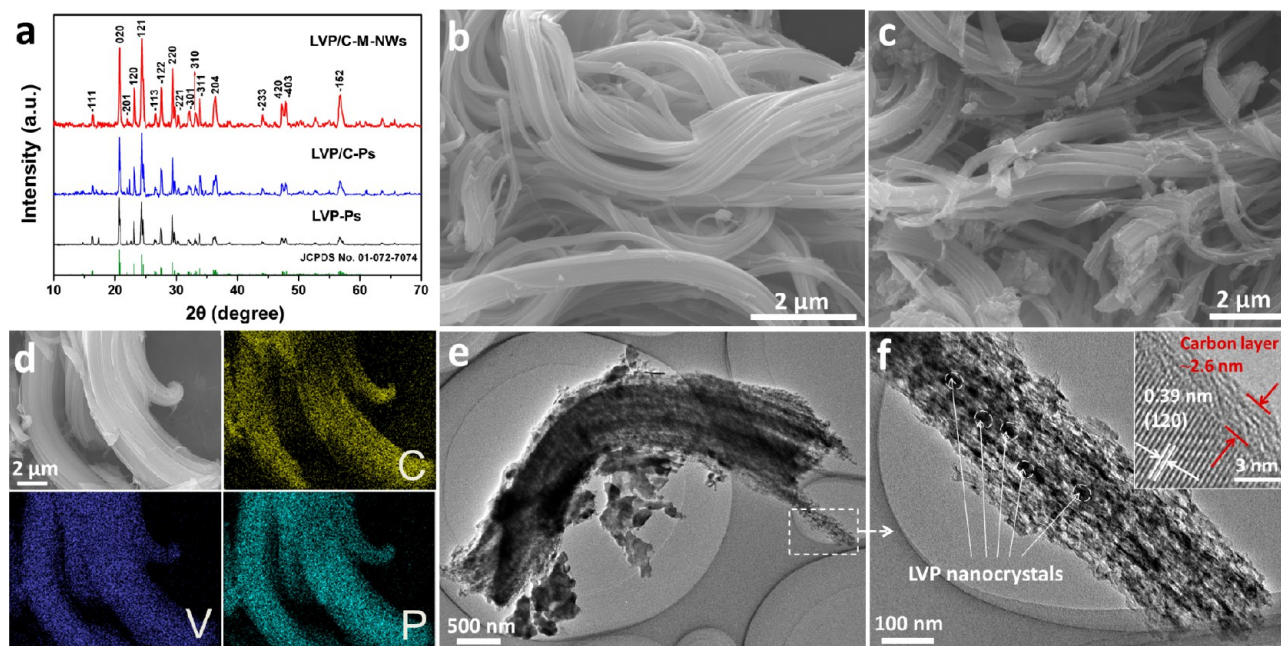
Figure 2. (a) XRD patterns of the LVP/C-M-NWs, LVP/C-Ps and LVP-Ps, respectively. (b) SEM image of the LVP nanowire precursor. (c–f) SEM image (c), elemental mapping images (d), and TEM images (e,f) of LVP/C-M-NWs; inset of (f) is the HRTEM image.
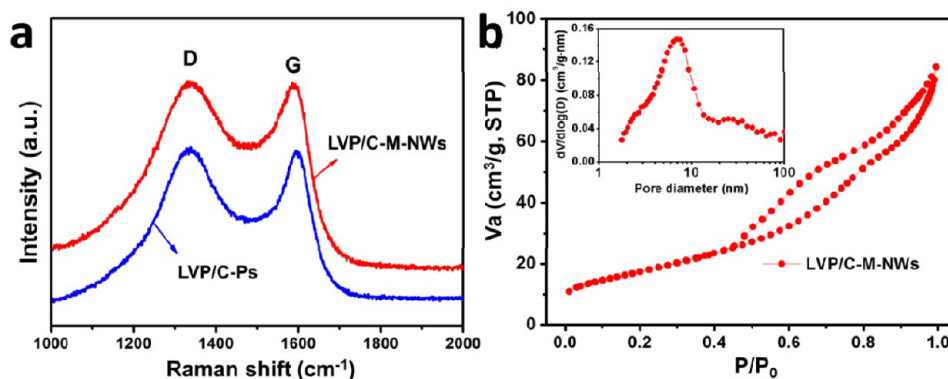

Figure 3. (a) Raman spectra of the LVP/C-M-NWs and LVP/C-Ps, respectively. (b) Nitrogen adsorption−desorption isotherm of the LVP/C-M-NWs; inset is the corresponding pore-size-distribution curve.

synthesized without adding any surfactants (Supporting Information Figures S1c and S5).

The X-ray diffraction (XRD) patterns (Figure 2a) of the three samples clearly indicate the formation of a high crystalline phase after annealing. All diffraction peaks are indexed to the monoclinic LVP phase (space group: $P2_1/n$) with lattice constants $a = 8.606$ Å, $b = 8.592$ Å, $c = 12.037$ Å, and $\beta = 90.61°$ (JCPDS No. 01-072-7074), indicating the high purity of the as-synthesized samples. Scanning electron microscopy (SEM) and transmission electron microscopy (TEM) were used to characterize the morphology and detailed structure of samples. The morphology of nanowire precursor is bundles of nanowires (Figure 2b). The elemental mapping images display the existence and uniform distribution of C, V, and P (Supporting Information Figure S6), demonstrating the precursory nanowires are composed of organic surfactant and hydrolyzed LVP colloids. After annealing, the nanowires are preserved (Figure 2c). The diameter of single nanowire ranges from 100 to 250 nm, and the length is up to tens of micrometers. Further, the elemental mapping images confirm

the uniform distribution of C, V, and P in the LVP/C-M-NWs as well (Figure 2d). The TEM images (Figure 2e,f) indicate that LVP nanocrystals and pores are distributed in the nanowires. The high-resolution TEM (HRTEM) image displays a lattice fringe with d-spacing of 0.39 nm, corresponding to the (120) planes of monoclinic LVP crystal, and an amorphous carbon layer of ∼2.5 nm contacting to the LVP crystal (Figure 2f, inset). For the LVP/C-Ps, particles with irregular sizes were observed (Supporting Information Figure S3b). The TEM image (Supporting Information Figure S3c) shows that the composed LVP crystals are bigger than those in the LVP/C-M-NWs, and ∼7 nm amorphous carbon shells are coated on the particles (Supporting Information Figure S3d).

Raman spectra were recorded to further study the nature of carbon formed in the samples (Figure 3a). The characteristic signatures located at around 1350 and 1600 cm^{-1} are attributed to the D-band (originating from disordered carbon) and G-band (graphitic carbon), respectively, indicating that the mesoporous and coated carbon are partially graphitized.[41,42] Nitrogen sorption isotherms were generated to investigate the
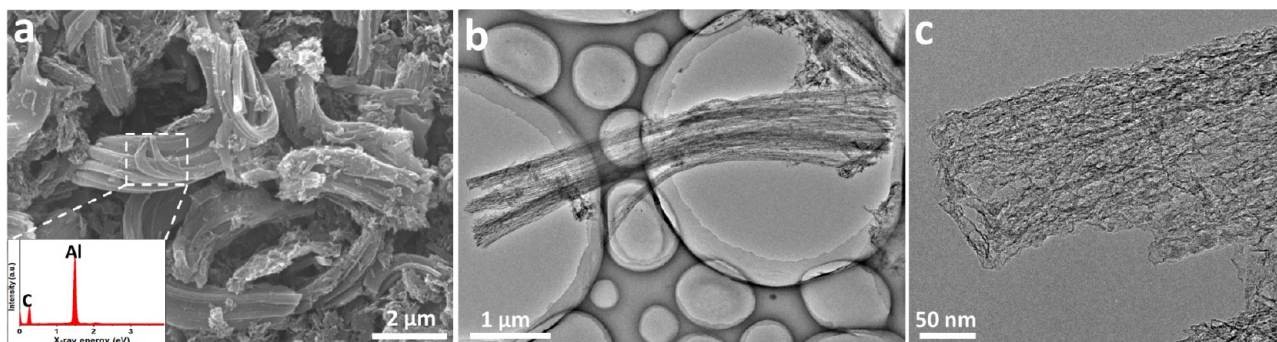
Figure 4. SEM image (a) and TEM images (b,c) of the residual mesoporous carbon after removing the LVP in LVP/C-M-NWs; the inset of (a) is the EDX spectrum of selected region.
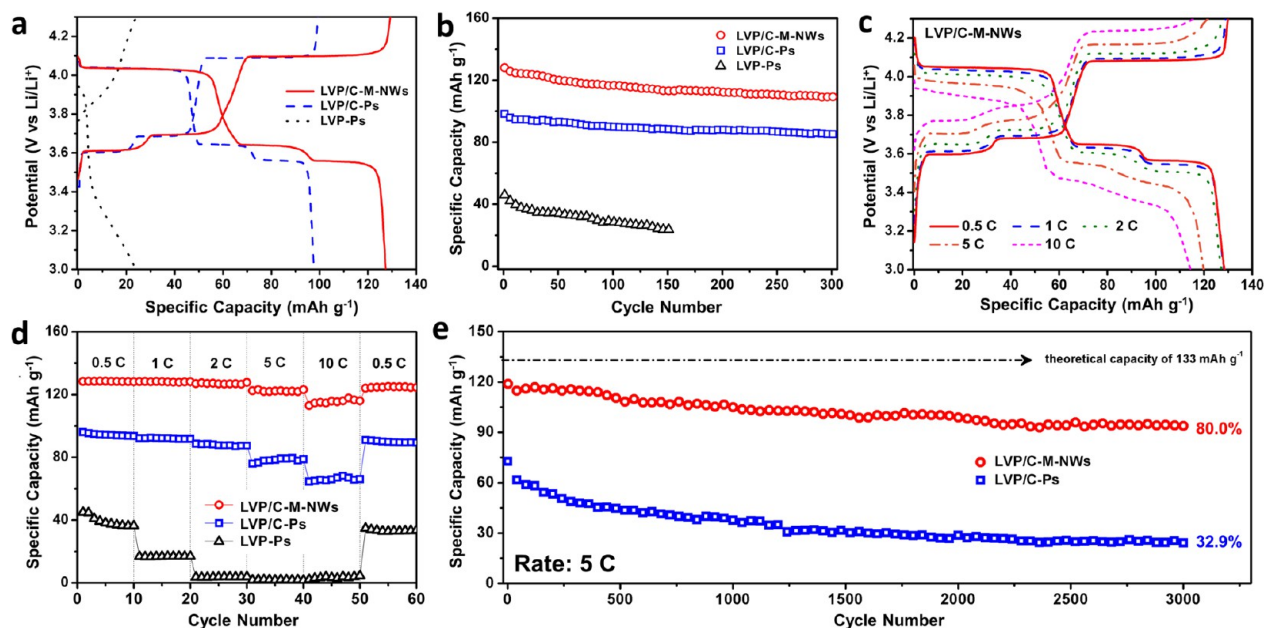

Figure 5. Electrochemical characteristics: (a) Charge–discharge profiles and (b) cycling performance of the LVP/C-M-NWs, LVP/C-Ps, and LVP-Ps cathodes at 1 C in 3–4.3 V, respectively. (c) Charge–discharge profiles of the LVP/C-M-NWs cathode at different current rates. (d) Rate performance of the LVP/C-M-NWs, LVP/C-Ps, and LVP-Ps cathodes, respectively. (e) Ultralong-life cycling performance of the LVP/C-M-NWs and LVP/C-Ps at 5 C.

Brunauer−Emmet−Teller (BET) surface area and the porous structure of the samples. The BET surface area of LVP/C-M-NWs is 65.1 m^2 g^{-1}, which is over ten times larger than that of LVP/C-Ps (6.1 m^2 g^{-1}), while the BET surface area of LVP-Ps is only 0.06 m^2 g^{-1}. The nitrogen adsorption−desorption curve of LVP/C-M-NWs (Figure 3b) exhibits a typical hysteresis (type-IV).[35] The Barret−Joyner−Halenda (BJH) pore-size-distribution curve (Figure 3b, inset) displays that the pore sizes in LVP/C-M-NWs are mainly below 10 nm with pore volume of ∼0.127 cm^3 g^{-1}. However, the LVP/C-Ps exhibit a large and wide pore distribution with pore volume of ∼0.044 cm^3 g^{-1} (Supporting Information Figure S7).

Since the mesoporous nanowires were synthesized in one pot along with the *in situ* carbonization of organic surfactants, the carbon structure formed in LVP/C-M-NWs need to be clearly investigated. To completely remove the LVP crystals, the LVP/C-M-NWs were dipped in hydrofluoric acid three days along with intermittently ultrasonic treatment and then washed by deionized water and ethanol three times. The energy-dispersive X-ray (EDX) analysis (inset of Figure 4a) demonstrates that LVP crystals are totally removed and only carbon remains (the

Al element comes from the substrate). The morphology of bundled nanowires is largely retained (Figure 4). The TEM images (Figure 4b,c) indicates that the carbon scaffolds are mesopores. However, for LVP/C-Ps, the residual carbon from the coating shells are nanosheets (Supporting Information Figure S8). Determined from thermogravimetric (TG) analysis (Supporting Information Figure S9), the carbon content of LVP/C-M-NWs and LVP/C-Ps is 9.7 and 4.5 wt.%, respectively, which is consistent with the mass ratio of the residual carbon. Furthermore, BET surface area of the residual mesoporous carbon is as high as 990 m^2 g^{-1}. Another pore size distribution around 30 nm is probably attributed to the removal of LVP nanocrystals (Supporting Information Figure S10), which is consistent with the TEM image of LVP/C-M-NWs (Figure 2f) and mesoporous carbon (Figure 4c). The above results demonstrate that the carbon formed in the nanowires is mesoporous with continuous pores and good structure stability (this structure is not destroyed after removing LVP). Meanwhile, the LVP nanocrystals are uniformly embedded in the mesoporous nanowires and tightly contact with the carbon scaffolds, forming the hierarchical LVP/C-M-NWs.
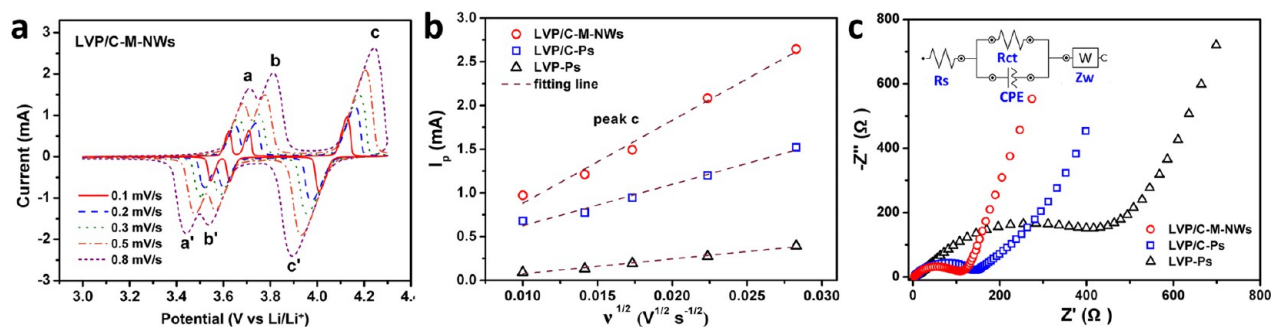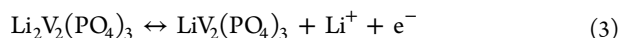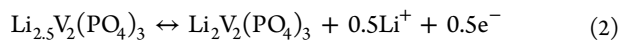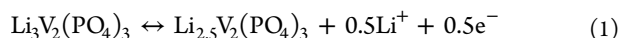
Figure 6. (a) Cyclic voltammogram of LVP/C-M-NWs cathode at different scan rates. (b) Linear fitting of I_p vs $v^{1/2}$ curves for the peak c. (c) The Nyquist plots of the LVP/C-M-NWs, LVP/C-Ps, and LVP-Ps cathodes after three full cycles at 1 C, respectively.

The lithium storage performances were investigated by using coin-type cells.[43] When cycled at a rate of 1 C (1 C = 133 mAh g^{-1}) in 3−4.3 V (Figure 5a), the carbon modified samples, LVP/C-M-NWs and LVP/C-Ps, both exhibit three pairs of charge/discharge plateaus located at around 3.61/3.55, 3.69/3.63, and 4.09/4.03 V, owing to a series of reversible phase transitions during electrochemical reactions (eqs 1−3), respectively.[8,10]

$$Li_3V_2(PO_4)_3 \leftrightarrow Li_{2.5}V_2(PO_4)_3 + 0.5Li^+ + 0.5e^- \qquad (1)$$

$$Li_{2.5}V_2(PO_4)_3 \leftrightarrow Li_2V_2(PO_4)_3 + 0.5Li^+ + 0.5e^- \qquad (2)$$

$$Li_2V_2(PO_4)_3 \leftrightarrow LiV_2(PO_4)_3 + Li^+ + e^- \qquad (3)$$

However, no clear flat plateau is observed for LVP-Ps cathode. The initial discharge capacity of LVP/C-M-NWs cathode is 128 mAh g^{-1} (extremely close to the theoretical capacity of 133 mAh g^{-1} in 3−4.3 V), higher than that of LVP/C-Ps (98 mAh g^{-1}) and LVP-Ps (46 mAh g^{-1}). After 300 cycles, the capacity retention of LVP/C-M-NWs and LVP/C-Ps cathode is 89.8 and 86.1%, respectively (Figure 5b). For LVP-Ps, the capacity fast fades to 50% of its initial value after 150 cycles.

Rate performance of the three samples was further compared. With the rate increasing (Figure 5c,d and Supporting Information Figures S11 and S12), the LVP/C-M-NWs cathode exhibits the smallest capacity decrease among the three samples. Even at 10 C, a discharge capacity of 117 mAh g^{-1} (88.0% of the theoretical capacity) is still delivered, almost two times that of the LVP/C-Ps cathode (64 mAh g^{-1}), indicating the excellent high-rate capability. After rapid changes of the current rate, the LVP/C-M-NWs cathode shows stable capacities at each state (Figure 5d). When rate is turned back to 0.5 C, about 97.7% of the initial capacity for LVP/C-M-NWs cathode is recovered, better than that of LVP/C-Ps cathode (92.7%). But the LVP-Ps cathode displays almost no capacity at high rate. Long-life cycling performance of samples at high rate of 5 C is subsequently shown in Figure 5e. The LVP/C-M-NWs cathode exhibits an initial discharge capacity of 120 mAh g^{-1}, and delivers a remarkable capacity of 107 mAh g^{-1} after 1000 cycles, corresponding to capacity retention of 89.2%. It is worth noting that more than 80.0% capacity is still remained after 3000 cycles, much better than that of LVP/C-Ps cathode (32.9%). The specific capacity and cycling stability for LVP/C-M-NWs cathode are better than the state-of-the-art reported LVP cathodes.[10,29,44,45]

To reveal the reason of the enhanced electrochemical performance for mesoporous nanowire composites, cyclic voltammetry (CV) and electrochemical impedance spectra

(EIS) as well as the morphology changes of samples before/after cycling were measured. With the increasing scan rate, the peak current increases, meanwhile the cathodic and anodic peaks shift to lower and higher potentials, respectively (Figure 6a). Comparing with the peaks shifting of LVP/C-Ps and LVP-Ps cathodes (Supporting Information Figure S13), the LVP/C-M-NWs cathode still undergoes three complete phase transitions. The current of LVP/C-M-NWs is the highest among the three samples, indicating its highest reversibility and fastest kinetics during electrochemical reaction.[10] Based on the Randles Sevchik equation (eq 4) for semi-infinite diffusion of Li$^+$ into LVP, the apparent diffusion coefficients were calculated.[44]

$$I_p = 2.69 \times 10^5 n^{3/2} A C_0 D^{1/2} v^{1/2} \qquad (4)$$

where I_p is the peak current, n is the number of electrons transferred per molecule, A is the active surface area of the electrode, C_0 is the concentration of lithium ions in the cathode, D is the apparent ion diffusion coefficient, and v is the scanning rate. From the slope of the fitting line collected from the peak c (Figure 6b), the apparent diffusion coefficient D of LVP/C-M-NWs is 4.11×10^{-9} cm^2 s^{-1}, higher than those of LVP/C-Ps (1.03×10^{-9} cm^2 s^{-1}) and LVP-Ps (1.30×10^{-10} cm^2 s^{-1}), respectively. The Nyquist plots (Figure 6c) show that the charge transfer resistance (R_{ct}) of both carbon modified products, LVP/C-M-NWs (103 Ω) and LVP/C-Ps (135 Ω), are much smaller than that of LVP-Ps (410 Ω). This indicates that carbon modification indeed improves the charge transfer kinetics.[16−18] However, the R_{ct} of LVP/C-M-NWs is smaller than that of LVP/C-Ps, demonstrating that the mesoporous nanowires provide higher efficient electron/ion transport than that of the carbon coating. The SEM images of LVP/C-Ps and LVP/C-M-NWs cathodes before and after cycling are shown in Supporting Information Figures S14 and S15, respectively. Under long-term cycling test, the bulk particles aggregate or pulverize caused by volume variations, leading to the instable interface, loss of electrical contact between active mass and current collector, and the capacity fading (Supporting Information Figure S14).[26,27] In this case, the morphology of LVP/C-M-NWs displays negligible change even after 300 cycles at 1 C (Supporting Information Figure S15), which demonstrates the mesoporous nanowire structure promptly accommodate the volume variations during cycling.

On the basis of the above results, the superior high-rate and long cycling performance of LVP/C-M-NWs is attributed to the advantages of hierarchical mesoporous nanowires, as illustrated in Figure 1a. First, the conductive carbon mesoporous nanowire offers continuous electron transport

pathway; simultaneously, the mesoporous channels provide rapid ion diffusion pathways. Also the large surface area (65.1 $m^2 g^{-1}$) and mesopores increase the electrode−electrolyte contact area. Thus, the bicontinuous electron/ion transport pathways greatly facilitate the ion diffusion kinetics (Figure 6a,b) and reduce the R_{ct} (Figure 6c), resulting in the excellent rate capability. Second, the mesoporous nanowires with uniform distribution of LVP nanocrystals (Figure 2c−e) reduce the self-aggregation of active materials and the stable mesoporous structure can rapidly accommodate the volume variations during repeated Li$^+$ extraction/insertion,[30−33] which guarantee the effective electron contact upon prolonged cycling, leading to the attractive structure stability (Supporting Information Figure S15) and remarkable ultralong cycle life.

In summary, we have developed a convenient one-pot strategy to synthesize novel mesoporous nanowire structure (LVP/C-M-NWs) by using CTAB and oxalic acid as surfactants. This approach is facile and cost-saving since the mesoporous composite is directly *in situ* carbonized from the surfactant along with the crystallization of LVP without using any hard templates. Such novel LVP/C-M-NWs architecture provides bicontinuous electron/ion pathways and large electrode−electrolyte contact area for rapid Li$^+$ diffusion and electron transport. Meanwhile the robust structure stability facilitates the strain relaxation upon prolonged cycling. These advantages lead to the excellent rate capability and ultralong-life cycling stability. This kind of novel mesoporous nanowire structure and the effective strategy can be further applied to the high-performance energy storage devices.

■ ASSOCIATED CONTENT

Ⓢ Supporting Information

Additional information and figures. This material is available free of charge via the Internet at http://pubs.acs.org.

■ AUTHOR INFORMATION

Corresponding Author

*E-mail: mlq518@whut.edu.cn.

Author Contributions

§These authors contributed equally to this work.

Notes

The authors declare no competing financial interest.

■ ACKNOWLEDGMENTS

■ REFERENCES

(1) Gogotsi, Y.; Simon, P. *Science* **2011**, *334*, 917−918.
(2) Kang, B.; Ceder, G. *Nature* **2009**, *458*, 190−193.
(3) (a) Aricò, A. S.; Bruce, P.; Scrosati, B.; Tarascon, J. M.; Van Schalkwijk, W. *Nat. Mater.* **2005**, *4*, 366−377. (b) Dunn, B.; Kamath, H.; Tarascon, J. M. *Science* **2011**, *334*, 928−935.

(4) Goodenough, J. B.; Park, K. S. *J. Am. Chem. Soc.* **2013**, *135*, 1167−1176.
(5) Chan, C. K.; Peng, H.; Liu, G.; McIlwrath, K.; Zhang, X. F.; Huggins, R. A.; Cui, Y. *Nat. Nanotechnol.* **2007**, *3*, 31−35.
(6) Bruce, P. G.; Scrosati, B.; Tarascon, J. M. *Angew. Chem., Int. Ed.* **2008**, *47*, 2930−2946.
(7) Masquelier, C.; Croguennec, L. *Chem. Rev.* **2013**, *113*, 6552−6591.
(8) Mai, L.; Li, S.; Dong, Y.; Zhao, Y.; Luo, Y.; Xu, H. *Nanoscale* **2013**, *5*, 4864−4869.
(9) Kim, J.; Yoo, J. K.; Jung, Y. S.; Kang, K. *Adv. Energy Mater.* **2013**, *3*, 1004−1007.
(10) Su, J.; Wu, X.-L.; Lee, J.-S.; Kim, J.; Guo, Y.-G. *J. Mater. Chem. A* **2013**, *1*, 2508−2514.
(11) Chen, J.; Duan, W.; Hu, Z.; Zhang, K.; Cheng, F.; Tao, Z. *Nanoscale* **2013**, *5*, 6485−6490.
(12) Yin, S.-C.; Grondey, H.; Strobel, P.; Huang, H.; Nazar, L. F. *J. Am. Chem. Soc.* **2003**, *125*, 326−327.
(13) Huang, H.; Yin, S. C.; Kerr, T.; Taylor, N.; Nazar, L. F. *Adv. Mater.* **2002**, *14*, 1525−1528.
(14) Lee, S.; Park, S. S. *J. Phys. Chem. C* **2012**, *116*, 25190−25197.
(15) Yin, S. C.; Grondey, H.; Strobel, P.; Anne, M.; Nazar, L. *J. Am. Chem. Soc.* **2003**, *125*, 10402−10411.
(16) Shen, L.; Li, H.; Uchaker, E.; Zhang, X.; Cao, G. *Nano Lett.* **2012**, *12*, 5673−5678.
(17) Li, H.; Zhou, H. *Chem. Commun.* **2012**, *48*, 1201−1217.
(18) Xin, S.; Guo, Y. G.; Wan, L. J. *Acc. Chem. Res.* **2012**, *45*, 1759−1769.
(19) (a) Zhang, H.; Yu, X.; Braun, P. V. *Nat. Nanotechnol.* **2011**, *6*, 277−281. (b) Pikul, J. H.; Zhang, H. G.; Cho, J.; Braun, P. V.; King, W. P. *Nat. Commun.* **2013**, *4*, 1732. (c) Zhang, H.; Braun, P. V. *Nano Lett.* **2012**, *12*, 2778−2783.
(20) (a) Kempa, T. J.; Day, R. W.; Kim, S. K.; Park, H. G.; Lieber, C. M. *Energy Environ. Sci.* **2013**, *6*, 719−733. (b) Kim, S. K.; Day, R. W.; Cahoon, J. F.; Kempa, T. J.; Song, K. D.; Park, H. G.; Lieber, C. M. *Nano Lett.* **2012**, *12*, 4971.
(21) Hochbaum, A. I.; Chen, R. K.; Delgado, R. D.; Liang, W. J.; Garnett, E. C.; Najarian, M.; Majumdar, A.; Yang, P. D. *Nature* **2007**, *451*, 163−168.
(22) (a) Mai, L. Q.; Yang, F.; Zhao, Y. L.; Xu, X.; Xu, L.; Luo, Y. Z. *Nat. Commun.* **2011**, *2*, 381. (b) Yan, M.; Wang, F.; Han, C.; Ma, X.; Xu, X.; An, Q.; Xu, L.; Niu, C.; Zhao, Y.; Tian, X. *J. Am. Chem. Soc.* **2013**, *135*, 18176.
(23) (a) Zhu, C.; Yu, Y.; Gu, L.; Weichert, K.; Maier, J. *Angew. Chem., Int. Ed.* **2011**, *50*, 6278−6282. (b) Chen, Q.; Zhang, T.; Qiao, X.; Li, D.; Yang, J. *J. Power Sources* **2013**, *234*, 197−200.
(24) (a) Zhao, Y. L.; Xu, L.; Mai, L. Q.; Han, C. H.; An, Q. Y.; Xu, X.; Liu, X.; Zhang, Q. J. *Proc. Natl. Acad. Sci. U.S.A.* **2012**, *109*, 19569−19574. (b) Xu, J.; Wu, H.; Wang, F.; Xia, Y.; Zheng, G. *Adv. Energy Mater.* **2013**, *3*, 286−289.
(25) (a) Wang, B.; Li, X.; Zhang, X.; Luo, B.; Jin, M.; Liang, M.; Dayeh, S. A.; Picraux, S.; Zhi, L. *ACS Nano* **2013**, *7*, 1437−1445. (b) Evanoff, K.; Benson, J.; Schauer, M.; Kovalenko, I.; Lashmore, D.; Ready, W. J.; Yushin, G. *ACS Nano* **2012**, *6*, 9837−9845.
(26) (a) Zhang, X.; Cheng, F.; Yang, J.; Chen, J. *Nano Lett.* **2013**, *13*, 2822−2825. (b) Luo, C.; Xu, Y.; Zhu, Y.; Liu, Y.; Zheng, S.; Liu, Y.; Langrock, A.; Wang, C. *ACS Nano* **2013**, *7*, 8003−8010.
(27) Mai, L. Q.; Wei, Q. L.; An, Q. Y.; Tian, X. C.; Zhao, Y. L.; Xu, X.; Xu, L.; Chang, L.; Zhang, Q. J. *Adv. Mater.* **2013**, *25*, 2969−2973.
(28) (a) Arruda, T. M.; Heon, M.; Presser, V.; Hillesheim, P. C.; Dai, S.; Gogotsi, Y.; Kalinin, S. V.; Balke, N. *Energy Environ. Sci.* **2013**, *6*, 225−231. (b) Tsai, W. Y.; Gao, P. C.; Daffos, B.; Taberna, P. L.; Perez, C. R.; Gogotsi, Y.; Favier, F.; Simon, P. *Electrochem. Commun.* **2013**, *34*, 109−112.
(29) Du, X.; He, W.; Zhang, X.; Yue, Y.; Liu, H.; Zhang, X.; Min, D.; Ge, X.; Du, Y. *J. Mater. Chem.* **2012**, *22*, 5960−5969.
(30) (a) Mai, L. Q.; Minhas-Khan, A.; Tian, X. C.; Hercule, K. M.; Zhao, Y. L.; Lin, X.; Xu, X. *Nat. Commun.* **2013**, *4*, 2923. (b) Wang,

G.; Liu, H.; Liu, J.; Qiao, S.; Lu, G. M.; Munroe, P.; Ahn, H. *Adv. Mater.* **2010**, *22*, 4944−4948.

(31) Shen, L.; Zhang, X.; Uchaker, E.; Yuan, C.; Cao, G. *Adv. Energy Mater.* **2012**, *2*, 691−698.

(32) Liu, H.; Su, D.; Zhou, R.; Sun, B.; Wang, G.; Qiao, S. Z. *Adv. Energy Mater.* **2012**, *2*, 970−975.

(33) Shi, Y.; Hua, C.; Li, B.; Fang, X.; Yao, C.; Zhang, Y.; Hu, Y. S.; Wang, Z.; Chen, L.; Zhao, D. *Adv. Funct. Mater.* **2012**, *23*, 1832−1838.

(34) Pan, A. Q.; Wu, H. B.; Yu, L.; Lou, X. W. D. *Angew. Chem., Int. Ed.* **2013**, *125*, 2282−2286.

(35) Methods: the LVP/C-M-NWs was synthesized using V_2O_5, $NH_4H_2PO_4$, Li_2CO_3, oxalic acid, and cetyltrimethylammonium bromide (CTAB) as starting materials with a molar ratio of Li/V/P/oxalic acid/CTAB = 3:2:3:3:1. The synthesis process is shown in Supporting Information Figure S1. First, V_2O_5 and oxalic acid were dissolved in deionized water at 70 °C to form the VOC_2O_4 solution. Second, the mixed solution of $NH_4H_2PO_4$ and Li_2CO_3 were slowly dropped into the VOC_2O_4 solution. Third, the CTAB solution was dropped into the above solution under stirring. Finally, the solution was transferred to a Teflon lined autoclave and kept in an oven at 180 °C for 48 h. Then the final product was directly dried and annealed at 750 °C for 8 h in N_2. For comparison, the LVP/C-Ps was prepared without CTAB and annealed at 750 °C for 8 h in N_2. The LVP-Ps was prepared without CTAB and oxalic acid and annealed at 750 °C for 8 h in H_2 (5 vol. %)/Ar (95 vol. %). Characterization: XRD data were collected by a D8 Advance X-ray diffractometer, using Cu Kα radiation (λ = 1.5418 Å). The microstructures were observed by SEM (JEOL-7100F) and TEM (JEM-2100F). Raman spectra were obtained using a Renishaw INVIA micro-Raman spectroscopy system. TG analysis was performed using NETZSCH-STA449c/3/G thermoanalyzer. Brunauer-Emmet-Teller surface area was measured using Tristar II 3020 instrument by adsorption of nitrogen at 77 K.

(36) Zhao, D. Y.; Wan, Y.; Zhou, W. *Ordered Mesoporous Materials*; Wiley-VCH Verlag GmbH & Co. KGaA: Weinheim, Germany, 2013.

(37) Wan, Y.; Zhao, D. *Chem. Rev.* **2007**, *107*, 2821−2860.

(38) Wei, J.; Yue, Q.; Sun, Z.; Deng, Y.; Zhao, D. *Angew. Chem., Int. Ed.* **2012**, *51*, 6149−6153.

(39) (a) Zhong, W. B.; Liu, S. M.; Chen, X. H.; Wang, Y. X.; Yang, W. T. *Macromolecules* **2006**, *39*, 3224−3230. (b) El Haskouri, J.; Roca, M.; Cabrera, S.; Alamo, J.; Beltrán-Porter, A.; Beltrán-Porter, D.; Marcos, M. D.; Amorós, P. *Chem. Mater.* **1999**, *11*, 1446−1454.

(40) Li, W.; Yue, Q.; Deng, Y.; Zhao, D. *Adv. Mater.* **2013**, *25*, 5129−5152.

(41) Jian, Z.; Han, W.; Lu, X.; Yang, H.; Hu, Y. S.; Zhou, J.; Zhou, Z.; Li, J.; Chen, W.; Chen, D.; Chen, L. *Adv. Energy Mater.* **2013**, *3*, 156−160.

(42) Wu, X. L.; Jiang, L. Y.; Cao, F. F.; Guo, Y. G.; Wan, L. J. *Adv. Mater.* **2009**, *21*, 2710−2714.

(43) Electrochemical measurements. The electrochemical properties were characterized in coin cells with lithium metal foil as the anode. The cathode electrodes were composed of 70% active material, 20% acetylene black, and 10% poly(tetrafluoroethylene) (PTFE) binder. The electrode loading was 3−4 mg cm^{-2}. The electrolyte was composed of 1 M $LiPF_6$ dissolved in ethylene carbonate (EC)/dimethyl carbonate (DMC) with a volume ratio of 1:1. The cells were assembled in an argon-filled glovebox. Galvanostatic charge/discharge measurement was performed by a multichannel battery testing system (LAND CT2001A), cycling voltammetry (CV), and electrochemical impedance spectroscopy (EIS) were tested by an Autolab Potentiostat Galvanostat (PGSTAT302N). All the measurements were carried out at room temperature.

(44) Wang, H.; Li, Y.; Huang, C.; Zhong, Y.; Liu, S. *J. Power Sources* **2012**, *208*, 282−287.

(45) Wang, C.; Liu, H.; Yang, W. *J. Mater. Chem.* **2012**, *22*, 5281−5285.